Chinese Journal of Chemical Engineering 68 (2024) 203–215

Contents lists available at ScienceDirect

Chinese Journal of Chemical Engineering

journal homepage: www.elsevier.com/locate/CJChE

Full Length Article

Influence of syngas components and ash particles on the radiative heat transfer in a radiant syngas cooler

Chen Han [1,2], Youmin Situ [1,2], Huaxing Zhu [1,2], Jianliang Xu [1,2,*], Zhenghua Dai [1,2], Guangsuo Yu [1,2], Haifeng Liu [1,2]

[1] *National Energy Coal Gasification Technology Research and Development Center, East China University of Science and Technology, Shanghai 200237, China*

[2] *Shanghai Engineering Research Center of Coal Gasification, East China University of Science and Technology, Shanghai 200237, China*

ARTICLE INFO

Article history:
Received 3 August 2023
Received in revised form
13 December 2023
Accepted 21 December 2023
Available online 11 January 2024

Keywords:
Radiant syngas cooler
Weighted-sum-of-gray-gases model
Numerical simulation
Particle radiation

ABSTRACT

Radiant syngas cooler (RSC) is widely used as a waste heat recovery equipment in industrial gasification. In this work, an RSC with radiation screens is established and the impact of gaseous radiative property models, gas components, and ash particles on heat transfer is investigated by the numerical simulation method. Considering the syngas components and the pressure environment of the RSC, a modified weighted-sum-of-gray-gases model was developed. The modified model shows high accuracy in validation. In computational fluid dynamics simulation, the calculated steam production is only 0.63% in error with the industrial data. Compared with Smith's model, the temperature decay along the axial direction calculated by the modified model is faster. Syngas components are of great significance to heat recovery capacity, especially when the absorbing gas fraction is less than 10%. After considering the influence of particles, the outlet temperature and the proportion of radiative heat transfer are less affected, but the difference in steam output reaches 2.7 $t\cdot h^{-1}$. The particle deposition on the wall greatly reduces the heat recovery performance of an RSC.

1. Introduction

In the context of carbon peaking and carbon neutrality, the clean and efficient use of coal is promoted. As a key technology for clean coal utilization, entrained-flow gasification technology has been widely used in industry for its advantages of large operating load and high carbon conversion rate [1,2]. The gasifier syngas outlet temperature is usually above 1500 K, which must be cooled because the high temperature is inconvenient to transport [3,4]. Meanwhile, the cold gas efficiency of the coal–water–slurry (CWS) gasification process is generally around 75%, and a part of the energy exists in the high-temperature syngas and ash [5]. Radiant syngas cooler (RSC) is a kind of heat recovery equipment in which syngas and cooling water flow in reverse to produce high-grade steam [6]. Industrial practice shows that the RSC can effectively improve the thermal efficiency of gasification, and the operation is stable and reliable [7].

Due to the high-temperature and high-pressure working environment inside the RSC, it is unrealistic to conduct large-scale thermal experiments on it. Therefore, computational fluid dynamics (CFD) is the main method to study the flow and heat transfer processes inside the RSC. At present, research on the RSC mainly focuses on multiphase flow processes [8,9], structural optimization [10–12], and slag properties [13–15]. Radiative heat transfer is the main mode of heat transfer during the operation of the RSC, but there is a lack of research on the radiation characteristics of dusty gas inside the waste heat boiler. Syngas components in the RSC mainly include CO, H_2, H_2O and CO_2, of which H_2O and CO_2, as polar triatomic molecules, have strong radiation ability. At the same time, there is much CO in an RSC, and its radiation capacity cannot be ignored. The cost of accurately calculation of gas radiation characteristic parameters is huge, and it cannot be directly applied to CFD. Weighted-sum-of-gray-gases model (WSGGM) is a simplified gaseous radiative property model widely used in CFD, which greatly reduces computational costs [16]. However, the computational accuracy of WSGGM is limited, and it requires targeted corrections for different working conditions. In

* Corresponding author.
E-mail address: xujl@ecust.edu.cn (J. Xu).

https://doi.org/10.1016/j.cjche.2023.12.010
1004-9541/

the past, research on WSGGM mainly focused on oxy-fuel combustion [17–20].

Compared to boilers, the operating pressure of RSCs is higher and the gas composition varies greatly. The existing models cannot accurately calculate the multi-phase heat transfer process. The size of industrial RSC is large, which leads to its high cost [7]. To reduce the height of the RSC, it is necessary to carry out structure optimization and ash deposition study [9,21,22], which depends on the accurate prediction of the radiative heat transfer process in the RSC. Therefore, it is necessary to first modify the coefficients of the model based on the working environment of the RSC. The composition of the syngas in an RSC mainly depends on the operating conditions of the gasification process [23], including feeding mode, coal type, coal-slurry concentration, the ratio of oxygen to coal, and so on. With the progress of coal gasification, the composition of syngas will change [24]. This will have an impact on radiative heat transfer, and further affect steam output. Therefore, it is necessary to conduct research on the radiative heat transfer properties of RSCs under different syngas compositions. Meanwhile, the particle concentration in the RSC is much higher than that of the boiler [5,25], which has a greater impact on radiative heat transfer. It is important to study the contribution of particles to the heat transfer process in an RSC. There is currently a lack of research on gas radiation and particle heat transfer in an RSC. Conducting relevant research helps to further explore heat transfer enhancement methods in the RSC.

In this work, a three-dimensional model of an industrial-scale RSC is established and a modified WSGGM applicable to the RSC environment is proposed. The effect of gaseous radiative property models, syngas components, and fly ash particles on the heat transfer behavior inside the RSC is studied, and the results are compared with industrial data. The research results contribute to a better understanding of the heat transfer behavior inside the RSC and improve the accuracy of RSC simulation studies.

2. Model Description

2.1. Multiphase flow

2.1.1. Gas phase model

The gas–solid two-phase flow in the RSC has a low particle volume fraction, so an Euler–Lagrange method is generally adopted. In this work, syngas in the RSC is considered to be an incompressible ideal gas. To explain the gas flow behavior, the steady-state Navier–Stokes equation with the mass and energy conservation equations are solved.

$$\frac{\partial}{\partial(x_i)}(\rho\overline{u_i}) = S_\mathrm{m} \tag{1}$$

$$\frac{\partial}{\partial x_i}(\rho\overline{u_i}\overline{u_j}) = -\frac{\partial\overline{p}}{\partial x_j} + \frac{\partial}{\partial x_i}\left[\mu_\mathrm{t}\left(\frac{\partial\overline{u_i}}{\partial x_j} + \frac{\partial\overline{u_j}}{\partial x_i}\right)\right] + \frac{\partial}{\partial x_j}\left(-\rho\overline{u_i'u_j'}\right) + \rho g_i + S_{\mathrm{u}i} \tag{2}$$

$$\frac{\partial}{\partial x_i}(\rho\overline{u_j}\overline{h}) = \frac{\partial}{\partial x_i}\left(\frac{\lambda}{C_\mathrm{p}}\frac{\partial\overline{h}}{\partial x_i}\right) + S_\mathrm{rad} + S_\mathrm{h} \tag{3}$$

where $\overline{u}$, $\overline{p}$, and $\overline{h}$ are the mean velocity, pressure, and enthalpy of syngas, respectively; ρ, g and μ_t represent the density, acceleration of gravity, and turbulent viscosity, respectively; λ represents the thermal conductivity of fluid; and S_m, S_u, S_h, and S_rad represent the source terms of particle mass, momentum, enthalpy, and radiation, respectively. In the process of solving the equations above, a Reynolds stress model is necessary to solve the unknown term $\rho\overline{u_i'u_j'}$. Ni *et al.* [26] verified that the realizable k–ε model can accurately simulate the turbulent flow inside the RSC, so this paper uses it. The realizable k–ε model transport equations for the steady-state case are as follows:

$$\frac{\partial}{\partial x_i}(\rho\overline{u_i}k) = \frac{\partial}{\partial x_i}\left[\left(\mu + \frac{\mu_\mathrm{t}}{\sigma_k}\right)\frac{\partial k}{\partial x_i}\right] + G_k + G_b - \rho\varepsilon \tag{4}$$

$$\frac{\partial}{\partial x_i}(\rho\overline{u_i}\varepsilon) = \frac{\partial}{\partial x_i}\left[\left(\mu + \frac{\mu_\mathrm{t}}{\sigma_\varepsilon}\right)\frac{\partial\varepsilon}{\partial x_i}\right] + \rho C_1 S_\varepsilon - \rho C_2\frac{\varepsilon^2}{k + \sqrt{\nu\varepsilon}} + S_\varepsilon \tag{5}$$

where k and ε are the turbulent kinetic energy and turbulent dissipation rate; G_k and G_b represent the turbulent energy generated by the mean velocity gradient and buoyancy, respectively; $C_1 = \max[0.43,\ \eta/(\eta+5)]$. $\eta = Sk/\varepsilon$; σ_k and σ_ε are the turbulent Prandtl numbers of k and ε, respectively; and S_ε and ν represent the user-defined source term and kinematical viscosity. Detailed model parameters are shown in the Ref. [27].

2.1.2. Discrete phase model

In this work, the interactions between the gas and particles are considered, while the interactions between particles are neglected. The discrete random walk model is adopted to predict the motion of particles affected by the gas phase. It is assumed that there is no evaporation, devolatilization, or reaction processes of particles in an RSC. The energy conservation and momentum conservation equations of particles are given below:

$$m_\mathrm{dp}C_\mathrm{dp}\frac{\mathrm{d}T_\mathrm{dp}}{\mathrm{d}t} = A_\mathrm{dp}\frac{\lambda_\mathrm{dp}Nu}{d_\mathrm{dp}}\left(T - T_\mathrm{dp}\right) + A_\mathrm{dp}\varepsilon_\mathrm{dp}\sigma\left(\theta_\mathrm{R}^4 - T_\mathrm{dp}^4\right) + S_\mathrm{L} + S_\mathrm{e} \tag{6}$$

$$m_\mathrm{dp}\frac{du_\mathrm{dp}}{t} = \frac{1}{8}\frac{24f_\mathrm{d}}{Re_\mathrm{dp}}\pi d_\mathrm{dp}^2\rho\left|\overline{u} - u_\mathrm{dp}\right| + \frac{1}{6}\pi d_\mathrm{dp}^3\rho g\left(\rho_\mathrm{dp} - \rho\right) + F_\mathrm{S} \tag{7}$$

where C_dp, T_dp, and d_dp are heat capacity, temperature, and diameter of particles, respectively; λ_dp and Nu are thermal conductivity and Nusselt number, respectively; A_dp, ε_dp, σ, and θ_R are projected area, emissivity, Stefan–Boltzmann constant, and radiative temperature of particles, respectively; S_L and S_e are source term of phase change and other energy source terms; f_d and Re_dp are drag coefficient and Reynolds number; u_dp and ρ_dp are velocity and density of particles; F_S is additional force of particles. More detailed equations about particle motion are shown in Ref. [28].

In this work, the phase change process is considered during particle motion. An assumption is adopted that when the temperature is higher than the critical viscosity temperature (T_cv), the particles are regarded as the molten state. This assumption is widely adopted in solving molten slag flow problems [2]. Once the temperature of the particles reaches T_cv, all latent heat will be released into the continuous phase in the form of source term.

$$S_\mathrm{L} = \begin{cases} m_\mathrm{dp}L_\mathrm{dp},\ T_\mathrm{dp,0} > T_\mathrm{cv}\ \text{and}\ T_\mathrm{dp} \le T_\mathrm{cv} \\ 0,\ \text{others} \end{cases} \tag{8}$$

where L_dp represents the latent heat of slag; and $T_\mathrm{dp,0}$ represents the temperature of particles at entry to current cells.

2.2. Species transport model

The syngas contains several components, which are simulated using a species transport model that calculates the mass fraction of each component by solving the convective diffusion equation. There may be some reactions in the RSC, especially the syngas shift reaction [29]. Considering the low degree of reaction, this paper ignores them. The equation of the steady-state species transport model without considering chemical reactions is as follows:

$$\frac{\partial}{\partial t}(\rho Y_i) + \nabla(\rho \boldsymbol{u} Y_i) = -\nabla \boldsymbol{J}_i + S_i \tag{9}$$

where Y_i and $\boldsymbol{J}_i$ are the mass fraction and diffusion flux of specie i, respectively. S_i is the rate generated by the dispersed phase and user-defined sources.

2.3. Heat transfer model

2.3.1. Energy equation

The energy equation of steady state solved in ANSYS Fluent is given by:

$$\frac{\partial}{\partial t}(\rho E) + \frac{\partial}{\partial x_i}(u_i(\rho E + p)) = \frac{\partial}{\partial x_i}\left(\lambda_{\text{eff}}\frac{\partial T}{\partial x_i} - \sum_j h_j \boldsymbol{J}_j + u_j \tau_{ij\text{eff}}\right) + S_{\text{h}} \tag{10}$$

where E and p are mechanical energy and pressure; λ_{eff} is the effective conductivity; and $\tau_{ij\text{eff}}$ is the effective viscous force. The first three terms on the right side express energy transfer due to conduction, species diffusion, and viscous dissipation, respectively.

2.3.2. Radiative transfer equation

In an RSC, heat transfer modes include conduction, convection, and radiation, of which radiation is the most important mode. The key to simulating radiative heat transfer is solving the radiative transfer equation (RTE). The RTE considering absorption, emission, and scattering of gases and particles are as follows:

$$\frac{\mathrm{d}I}{\mathrm{d}s} = \alpha\frac{\sigma T^4}{\pi} + E_{\text{dp}} - \left(\alpha + \alpha_{\text{dp}} + \sigma_{\text{dp}}\right)I + \frac{\sigma_{\text{dp}}}{4\pi}\int I(\boldsymbol{r}, \hat{s}')\varphi(\hat{s}, \hat{s}')\mathrm{d}\Omega' \tag{11}$$

where I represents the spectral radiation intensity; α represents the absorption coefficient of the gas mixture; α_{dp} and σ_{dp} represent the absorption coefficient and scattering coefficient of the particles, respectively; E_{dp} is the scattered energy; and $\varphi(\hat{s}, \hat{s}')$ is the phase function from $\hat{s}$ to $\hat{s}'$. The term on the left-side expresses the changing rate of light intensity along the direction of propagation. The first and second terms on the right side express the increase in light intensity due to gas emission and particle emission, respectively. The third term expresses the decrease in intensity due to absorption and scattering. The last term expresses the increase due to the reception of scattering in other directions.

In solving the radiative transfer equation, the P1 radiation model is chosen in this work. It is found that the model is fast in convergence and can be better applied to the study of RSC calculation [30].

2.3.3. The absorption and scattering coefficients

The sum of the proportions of H_2O and CO_2 in the syngas from CWS gasification is around 30%, and the proportion of CO is 30%–40%. For dry pulverized coal gasification with nitrogen pneumatic conveying, the proportion of H_2O and CO_2 in the syngas is as low as around 5%, while the proportion of CO reaches more than 60%. For RSC, especially with dry coal gasification, the effect of CO on radiation must be taken into account. More detailed information on gaseous radiative properties can be found in Refs. [31–33].

The absorption coefficient α of the gas mixture is calculated by the following equation:

$$\alpha = -\frac{1}{l}\ln(1 - \varepsilon_{\text{g}}) \tag{12}$$

where l is the path length, which is related to the size of the RSC. ε_{g} is the total emissivity of the gas mixture, which is related to various factors such as the properties of the gas mixture and the environment.

In WSGGM, ε is considered to be related to the gas components, temperature, pressure, and path length by the following equation:

$$\varepsilon_{\text{g}} = \sum_{i=0}^{n} a_i(T)\left(1 - \mathrm{e}^{-\kappa_i p l}\right) \tag{13}$$

where n represents the number of gray gases; a_i and κ_i represent the fraction and absorption coefficient of the ith gray gas, respectively; and p represents the total pressure of the absorbing gas.

In WSGGM, a_i is fitted as a single-valued function that is temperature-dependent.

$$a_i(T) = \sum_{j=1}^{J} b_{i,j}\left(\frac{T}{T_{\text{ref}}}\right)^{j-1} \tag{14}$$

where J is the number of polynomial terms and $b_{i,j}$ are polynomial coefficients. The reference temperature T_{ref} equals to 1200 K.

The ratio of partial pressure is defined below:

$$\text{Mr} = \frac{p_{H_2O}}{p_{CO_2}} \tag{15}$$

where p_{H_2O} and p_{CO_2} represent the partial pressure of water and carbon dioxide, respectively.

In this work, a WSGGM for RSC is developed. Corrections are made for the operating pressure and syngas composition of the RSC. The modified model is named WSGGM-RSC. A library of total emissivity is built relying on the benchmarks calculated by the line-by-line (LBL) method based on the HITEMP2010 database [34]. The WSGGM modified in this work is suitable for temperatures from 600 to 2500 K, and path lengths from 0.1 to 60 m. It is generally believed that there is no chemical reaction inside the RSC, so the syngas can be seen as homogeneous. The ratios of partial pressure Mr considered in this work include 1.0, 1.5 and 2.0. The Levenberg–Marquardt algorithm is used in the fitting process, and the details can be found in Ref. [19,35]. The polynomial coefficients of WSGGM-RSC are shown in Table 1. The way to implement WSGGM-RSC to CFD is shown in Table 2.

The absorption and scattering coefficients of particles are hard to determine. During coal combustion, the emissivity of particles is generally considered to be an empirical constant between 0.7 and 0.9 [36–38]. There are few studies on particle scattering factor, which has been recommended to be 0.9 [39], while 0.6 is another widely accepted value [40]. According to the study on residual particles of coal gasification by Mills and Rhine [41], the particle emissivity was selected as 0.83 in this work. When it comes to the scattering factor, Yin [42] gave a linear model depending on the fraction of unburnt combustibles,

Table 1
Coefficients of the WSGGM-RSC

i	k_i	$b_{i,1}$	$b_{i,2}$	$b_{i,3}$	$b_{i,4}$	$b_{i,5}$
Operating pressure = 6.5 MPa, Mr = 1.0, CO = 30% (vol)						
1	−0.5588	2.0437	−2.2887	1.1425	−0.2053	0.0052
2	0.6881	−2.2839	2.9686	−1.4921	0.2613	0.0531
3	0.2208	−0.5657	1.1884	−0.7078	0.1289	0.3650
4	0.5495	0.9567	−1.8278	0.9375	−0.1590	6.0999
Operating pressure = 6.5 MPa, Mr = 1.5, CO = 30% (vol)						
1	−0.5259	1.9633	−2.2451	1.1374	−0.2063	0.0054
2	0.6162	−2.0525	2.7106	−1.3799	0.2444	0.0509
3	0.2878	−0.8028	1.4405	−0.8061	0.1419	0.3652
4	0.5276	1.0459	−1.8905	0.9504	−0.1592	6.2506
Operating pressure = 6.5 MPa, Mr = 2.0, CO = 30% (vol)						
1	−0.5010	1.8954	−2.1926	1.1205	−0.2044	0.0056
2	0.5768	−1.9222	2.5645	−1.3158	0.2347	0.0499
3	0.3238	−0.9271	1.5692	−0.8549	0.1482	0.3693
4	0.5162	1.0863	−1.9113	0.9498	−0.1578	6.3548
Operating pressure = 4.0 MPa, Mr = 1.0, CO = 60% (vol)						
1	−1.2647	3.1221	−2.8771	1.1956	−0.1867	0.0124
2	−3.8662	5.3107	−3.2026	0.8857	−0.0924	0.1684
3	1.2540	−0.7530	−0.0411	0.1269	−0.0248	1.5508
4	1.4810	−3.3367	2.6112	−0.9218	0.1244	20.3156
Operating pressure = 4.0 MPa, Mr = 1.5, CO = 60% (vol)						
1	−1.1629	2.9643	−2.7744	1.1652	−0.1834	0.0130
2	−3.7431	5.0574	−2.9929	0.8095	−0.0821	0.1805
3	1.1182	−0.4818	−0.2298	0.1843	−0.0314	1.6041
4	1.5954	−3.5079	2.7114	−0.9485	0.1271	20.1406
Operating pressure = 4.0 MPa, Mr = 2.0, CO = 60% (vol)						
1	−1.0975	2.8493	−2.6891	1.1360	−0.1795	0.0134
2	−3.6405	4.8662	−2.8428	0.7567	−0.0751	0.1873
3	1.0098	−0.2934	−0.3527	0.2198	−0.0353	1.6261
4	1.6628	−3.5923	2.7502	−0.9552	0.1273	20.0171

Table 2
Way to use WSGGM-RSC in CFD

If (Mr ≤1.2)	Use coefficients for	Mr = 1.0
Else if (Mr ≤1.7)	Use coefficients for	Mr = 1.5
Else	Use coefficients for	Mr = 2.0

$$\sigma_{\text{dp}} = 0.9U_{\text{VM,C}} + 0.6(1 - U_{\text{VM,C}}) \tag{16}$$

where $U_{\text{VM,C}}$ represents the fraction of unburnt combustibles. For ash particles in RSC, the scattering factor equals 0.6.

2.3.4. Particle adhesion model

The industrial operation indicates that there is an increasing thickness of ash layer on the surface of the RSC membrane tube. Considering the low thermal conductivity of ash, the deposition process cannot be ignored. Therefore, an accurate dynamic particle adhesion model is necessary. In this work, when a particle in a molten state hits the wall, it is considered to be attached [3]. For solid particles, a critical velocity model (CVM) is adopted to determine adhesion characteristics, which has been validated in some research [3,14].

In CVM, the deposition of particles is determined by a critical velocity u_{cr}, which is related to the properties of the wall and particles [3].

$$u_{\text{cr}} = \left(\frac{2K}{d_{\text{dp}}B^2}\right)^{\frac{10}{7}} \tag{17}$$

where K is the effective stiffness coefficient; d_{dp} is the particle diameter; and B is the coefficient of motion recovery.

In addition, a critical angle, θ_{cr}, is used to further determine particle adhesion. If the angle between the direction of particle velocity and the normal direction of the wall is too large, then even if its velocity is less than the critical velocity, it is considered to rebound [43].

$$\theta_{\text{cr}} = \arctan\left(\frac{\mu_*}{\left(32\beta^3\right)^{0.5}}\sqrt{\frac{E^*}{G^*}}\right) \tag{18}$$

where μ_* is the effective friction coefficient; β is the effective coefficient of the contact radius; E^* and G^* are the effective Young's modulus and shear modulus of the particles, respectively.

In each wall cell, the shape of accumulated ash is assumed to be a cone. A large-scale detachment criterion based on the principles of mechanics is adopted to describe the shedding behavior when the thickness of accumulated ash achieves critical value [3,15].

$$F_{\text{D}}\delta_{\text{c}} \geq F_{\text{po}}R \tag{19}$$

where F_{D} and F_{po} are the drag force and van der Waals force of the accumulated ash, respectively; δ_{c} is the distance from the wall to the center of the cone; and R is the base area of a cone.

2.3.5. Equations of wall heat transfer

The heat transfer performance of the RSC wall determines its heat recovery ability. As shown in Fig. 1, heat is transferred from the gas phase to the cooling water through the ash layer and metal wall. In the process, the total heat flux, Q, is calculated by:

$$Q = kA_{\text{W}}\Delta T_{\text{W}} \tag{20}$$

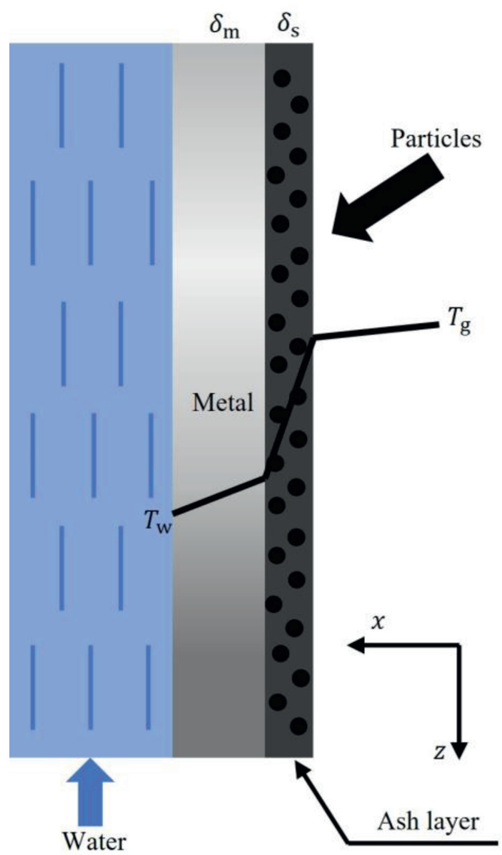

Fig. 1. Schematic diagram of wall heat transfer process.

where k is the heat transfer coefficient; A_W is the area of the cell; and ΔT_W is the temperature difference between ash layer and cooling water.

In the calculation process, k is related to properties of cooling water, metal wall, and ash layer.

$$k = \frac{1}{\frac{1}{h_{\text{conv}}} + \frac{\delta_m}{\lambda_m} + \frac{\delta_s}{\lambda_s}} \tag{21}$$

where h_{conv} is convective heat transfer coefficient of cooling water; δ_m and δ_s are the thickness of the metal wall and ash layer; and λ_m and λ_s are the thermal conductivity of the metal wall and ash layer.

In the problem of forced convection heat transfer in pipes, if the temperature difference is greater than 20–30 K, a correction factor needs to be introduced. The heat transfer coefficient considering the correction factor can be calculated by the following equation:

$$h_{\text{conv}} = 0.023 \times \frac{\lambda_f}{d} Re_f^{\,0.8} Pr_f^{\,0.4} \left(\frac{\eta_f}{\eta_w}\right)^{0.11} \tag{22}$$

where λ_f, Re_f, and Pr_f are thermal conductivity, Reynolds number, and Prandtl number of cooling water, respectively; η_f and η_w are dynamic viscosity calculated by average fluid temperature and wall temperature; and d is the diameter of tubes.

3. Boundary Condition and Mesh

3.1. Objects and working conditions

Fig. 2 shows the physical model adopted in this work, which is a part of industrial gasification process used in Yanzhou Coal Mining Yulin Energy Chemical Co., Ltd., Shaanxi, China. Considering that there are radiation screens arranged along the circumferential direction inside the RSC, a three-dimensional model is adopted. High-temperature syngas enters through the top inlet of the RSC with ash particles. The angle of the upper cone section is 30° and the angle of the lower cone section is 60°. Straight sections are distributed with radiation screens to enhance radiation efficiency. The width of the radiation screen is 285 mm and the size of the cooling tube is 57 mm × 7 mm. The ratio of height to diameter of RSC equals 7.8.

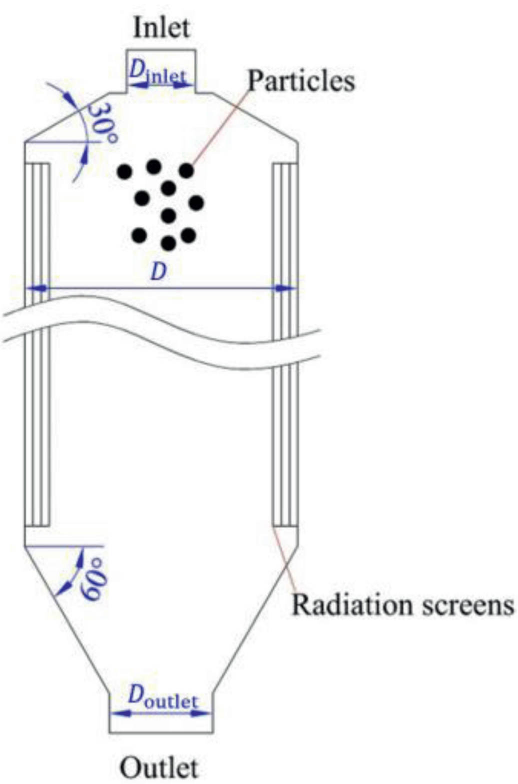

Fig. 2. Structure of the RSC.

Table 3
Boundary conditions

Parameter	CWS gasification	Dry coal gasification
Operating pressure/MPa	6.5	4.0
Inlet syngas temperature/°C	1340	1290
Inlet syngas mass flow rate/kg·h^{-1}	171936	160704
Syngas composition/% (mol)		
H_2O	20.38	7.47
CO_2	13.81	5.40
CO	37.31	63.46
H_2 and others	28.50	23.67

3.2. The mesh, methods, and boundary conditions

The boundary conditions and properties of inlet syngas and particles are shown in Tables 3 and 4. The gas temperature is measured by thermocouples, and the components are measured by gas chromatograph. The particle size is measured by a laser particle size analyzer, and the setting of physical properties refers to Refs. [12,44]. The temperature of the boiler water entering the water-cooled tube is 432 K, and the temperature of the saturated steam output from the steam drum is 571 K. In this work, the flow and heat transfer processes inside the RSC are considered steady-state processes.

The multiphase flow and heat transfer behavior of an industrial RSC is analyzed using numerical calculation methods by ANSYS Fluent software in this work. A mass-flow-rate inlet and a pressure outlet are adopted as inlet and outlet. A no-slip wall condition is adopted to set the wall. The particles in this work are assumed to follow a Rosin–Rammler distribution and a total of 37120 particles are tracked. Some other properties of syngas, like thermal conductivity, viscosity, and specific heat capacity, are defined by the mass-weighted mixing law. For single species, these properties are fitted to temperature-dependent polynomials. The computational domain is shown in Fig. 3. A 1/8 RSC model is established due to the symmetry, and a fine hexahedral mesh is applied to it. The grid near the wall and the radiation screen is encrypted, and the final grid number is around 850000. The SIMPLE algorithm, which couples pressure and velocity, is used for the solution. In the calculation, all terms are spatially discretized in second-order upwind format.

Table 4
Inlet ash and slag properties

Parameter	Slag	Ash
Particle density/kg·m^{-3}	2500	1060
Particle heat capacity/J·kg^{-1}·K^{-1}	1450	920
Particle thermal conductivity/W·m^{-1}·K^{-1}	1.87	0.25
T_{cv}/K	1457	
Latent heat/J·kg^{-1}	284000	
Mass flow rate/kg·h^{-1}	2592	6048
Mean diameter/mm	2.2	0.05
Minimum diameter/mm	0.1	0.001
Maximum diameter/mm	10	0.5
Spread parameter	0.68	1.23

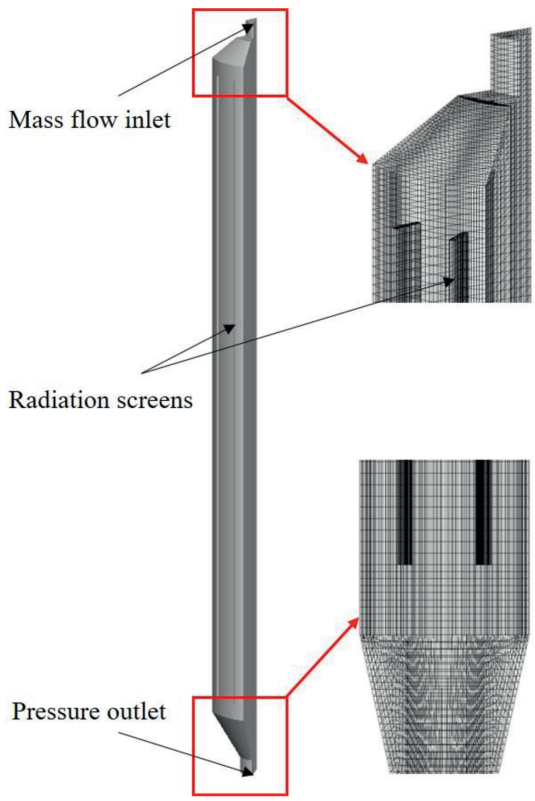

Fig. 3. Model and mesh.

4. Results and Discussion

4.1. Model accuracy verification

4.1.1. Grid independence verification

To eliminate the influence of grid numbers on the calculation results, a grid independence test is executed. Grid numbers of the RSC model considered in this work include 206748, 498222, 845582 and 1315224.

Fig. 4 shows the temperature distributions on the RSC axis for different grid numbers. Under low grid number conditions, the trends of temperature decreasing show a clear difference. When the grid number is more than 845582, it can be assumed that the number of grids does not affect the calculation results. Thus, the grid number in this work is chosen to be 845582.

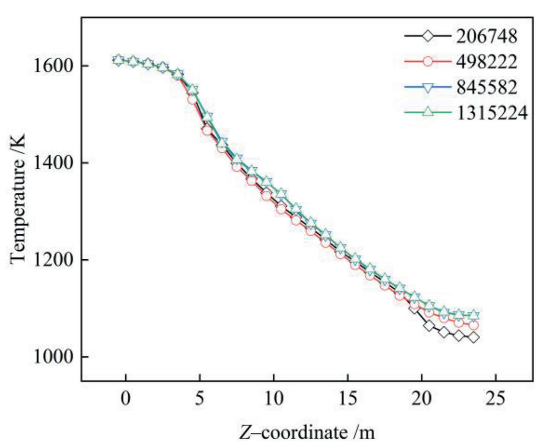

Fig. 4. Grid independence validation.

4.1.2. Model verified by the benchmark

In this section, the total emissivity of syngas under CWS and dry coal gasification conditions is calculated. To verify the accuracy of the new model, the calculation results of WSGGM-RSC and LBL are first compared.

As shown in Fig. 5, the overall total emissivity tends to decrease as the temperature rises under high pressure. The condition of Fig. 5(a) is consistent with CWS gasification, while Fig. 5(b) is closer to dry coal gasification. It can be seen that WSGGM-RSC calculates the total emissivity in good agreement with the LBL benchmarks. Fig. 6 exhibits the fitting quality of WSGGM-RSC at different path lengths. In most cases, the total emissivity calculated by WSGGM-RSC is in good accordance with LBL benchmarks. With the increase of path length, the total emissivity increases sharply at first. When the path length is larger than 1.5 m, the growth trend gradually flattens out.

Figs. 7 and 8 compare WSGGM-RSC with Smith's model, Yin's model, Johansson's model, and the LBL benchmarks. The results show that when the path length is larger than a certain value, the growth trend of the emissivity calculated by each WSGGM slows down sharply until it plateaus. For Smith's and Yin's models, this value is around 0.3 m. While for Johansson's model, this value is around 1 m. This result coincides with the range of pressure path

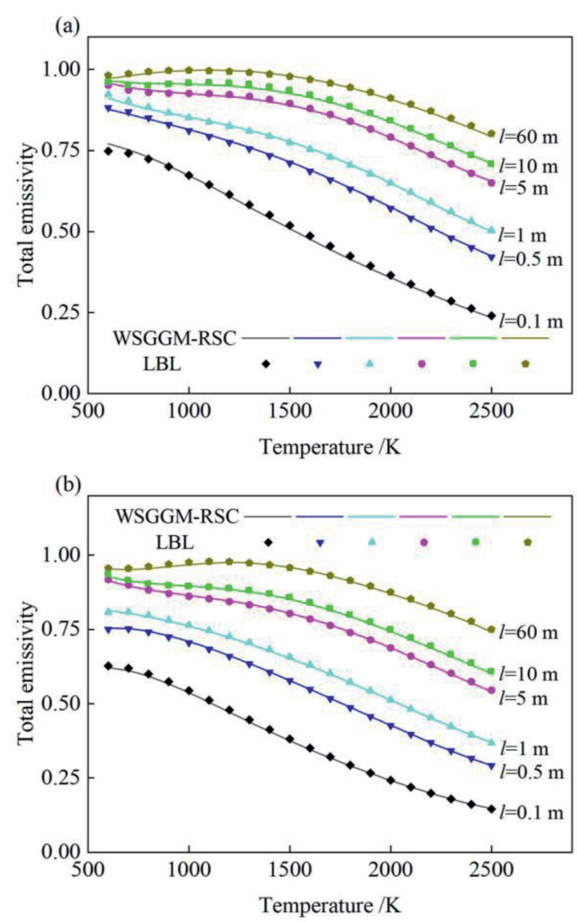

Fig. 5. Comparisons of total emissivity with temperature calculated by the WSGGM-RSC and LBL: (a) Mr = 1.0, p = 6.5 MPa; (b) Mr = 1.5, p = 4.0 MPa.

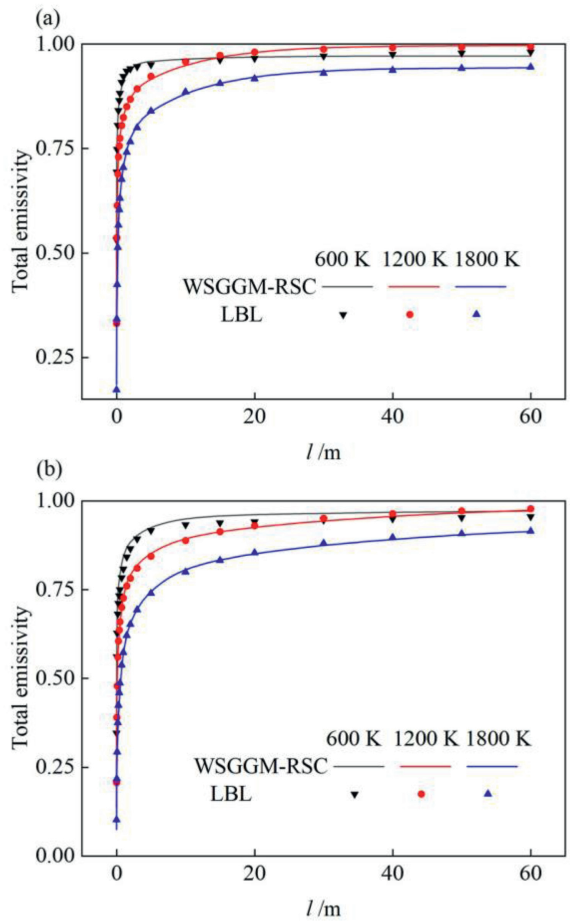

Fig. 6. Comparisons of total emissivity with path length calculated by the WSGGM-RSC and LBL: (a) Mr = 1.0, p = 6.5 MPa; (b) Mr = 1.5, p = 4.0 MPa.

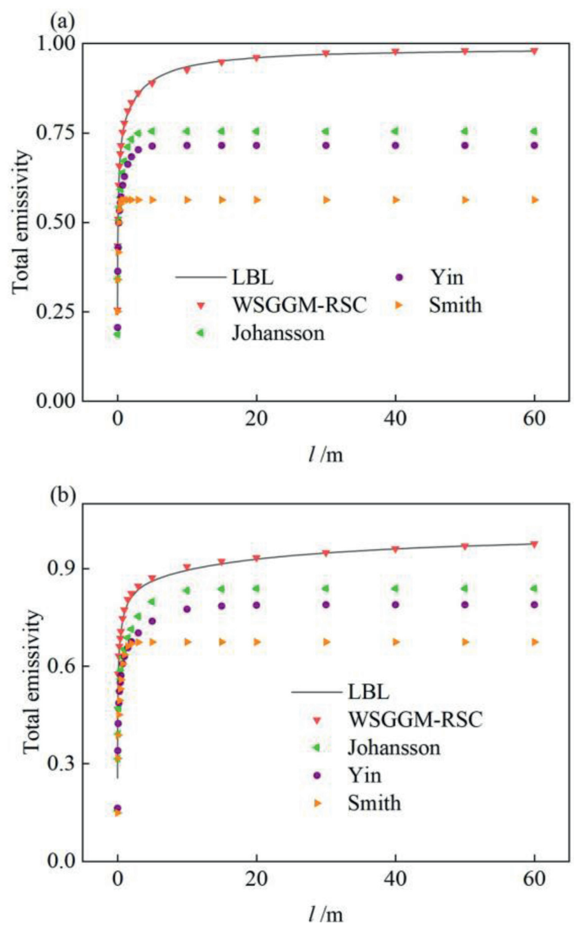

Fig. 7. Comparisons of total emissivity with path length calculated by WSGGM-RSC and other models: (a) p = 6.5 MPa, Mr = 1.0, T = 1500 K; (b) p = 4.0 MPa, Mr = 1.5, T = 1000 K.

applicability in Refs. [16–18], beyond which the model is distorted. Therefore, the difference between each model and the LBL benchmarks increases sharply while the path length is larger than 1 m. When the path length is larger than 1.5 m, the difference between the total emissivity calculated by each model and LBL is generally above 0.2 except for the new model. Only the new model shows a great agreement with the LBL at large path lengths. Usually, the radius of an RSC is about 1.5 m, and the average path length reaches about 2.5 m. In this situation, the deviation of the total emissivity calculated by other models tends to increase. A similar conclusion can be drawn from the comparison in Fig. 8. When the path length is large enough, the difference between WSGGM-RSC and other models is significant. The new model fits the LBL better than the other models at the internal temperature condition of the RSC.

In general, considering the effects of pressure, temperature, and path length, WSGGM-RSC shows advantages in predicting the total emissivity of the syngas inside the RSC.

4.1.3. Model verified by the industrial data

In this work, a simulation study is carried out for an industrial RSC of a CWS gasification process at the time of drive-up. It is considered that there is no ash accumulation on the wall. In the solution process, WSGGM-RSC, which replaces the default model, is adopted to predict the absorption coefficient of the gas mixture in the control volume.

The total steam production of the RSC calculated by CFD was counted and compared with the industrial production data. As shown in Fig. 9, the simulated values are quite close to the industrial data with an error of only 0.63% when WSGGM-RSC is applied and the particle radiation is considered.

The above verification illustrates that WSGGM-RSC can accurately calculate the absorption coefficient of syngas in the RSC. Therefore, WSGGM-RSC can be applied in the simulation of industrial RSC.

4.2. WSGGM-RSC applied in the simulation of industrial RSC

4.2.1. WSGGM-RSC compared to the default model in the CFD

In this work, WSGGM-RSC is applied to the CFD, and the results were compared with Smith's model. Fig. 10 shows the temperature distribution in the RSC calculated by numerical simulation. At the inlet of the RSC, there is a high-temperature region due to the jet core. The temperature difference between the different models near this region is small. At the end of the jet core, the temperature starts to decay sharply. In this region, less heat is absorbed by the membrane wall calculated by Smith's model due to its underestimation of syngas radiative capability. Therefore, the simulation results of WSGGM-RSC show a steeper temperature descent. As shown in Fig. 11, starting from the region of Z = 6 m, the calculated temperature decay of WSGGM-RSC along the axis is larger than that of Smith. In the lower half of the RSC, the temperature difference reaches about 20 K. The area with the highest temperature near the

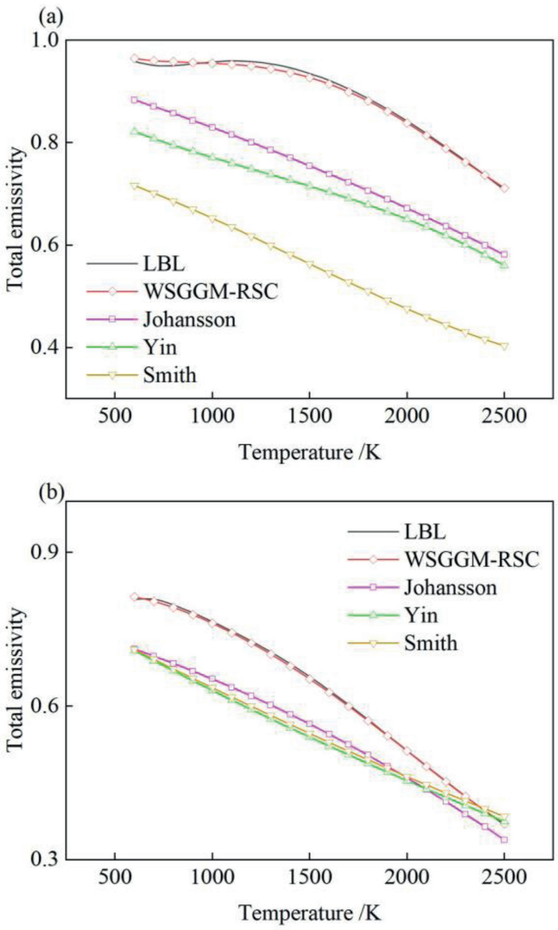

Fig. 8. Comparisons of total emissivity with temperature calculated by WSGGM-RSC and other models: (a) p = 6.5 MPa, Mr = 1.0, l = 10 m; (b) p = 4.0 MPa, Mr = 1.5, l = 1 m.

wall appears at the end of the jet core. In the lower part of the region, the temperature difference calculated by different models reached over 25 K.

The temperature difference can be explained by Fig. 12. Smith's model underestimates the effect of pressure on the syngas emissivity and therefore predicts a much lower absorption coefficient (about 0.6). In the CFD simulation, the absorption coefficient is a key parameter to calculate incident radiation and radiative temperature. As shown in Fig. 13, the incident radiation calculated by WSGGM-RSC is higher, especially at the jet core. WSGGM-RSC predicts the absorption coefficient more accurately. Therefore, the

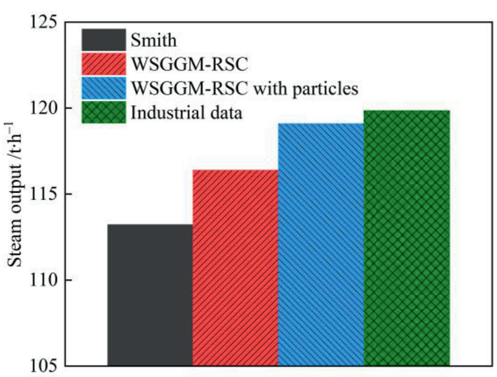

Fig. 9. Comparisons of the calculated steam output with the industrial data.

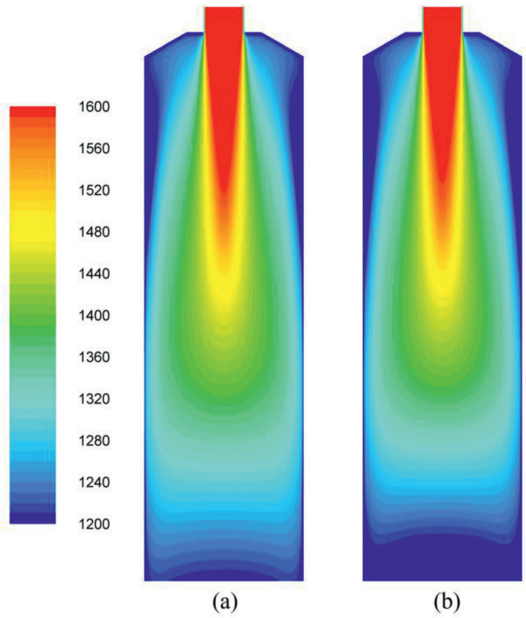

Fig. 10. Temperature contours in the center section of the RSC (unit K): (a) Smith's model, (b) WSGGM-RSC.

radiative capacity of the gas is corrected and more sensible heat is recovered, which leads to a larger temperature decay.

4.2.2. Radiative heat transfer behavior under different gas components

The effective gas of coal gasification includes H_2 and CO. With the development of gasification technology, the proportion of effective gas will increase, while the composition of H_2O and CO_2 will keep decreasing accordingly. This leads to changes in the radiative capacity of the syngas, which affects the heat recovery efficiency of the RSC. In this section, the effect of the gas components on the heat recovery capacity of the RSC is discussed.

The total emissivity calculated by WSGGM-RSC for different absorbing gas fractions is first compared. As shown in Fig. 14, the total emissivity calculated for different partial pressure ratios at a temperature of 1300 K and a path length of 2.5 m does not show a large difference. As the mole fraction of $H_2O + CO_2$ increases, the total emissivity first increases sharply. When the fraction of absorbing gas reaches more than 10%, the increasing trend becomes slow. According to the results calculated by WSGGM-RSC, the radiation capacity of the syngas fluctuates considerably when the absorbing gas component is below 10%. Accordingly, the heat recovery capacity of the RSC will be greatly affected.

The CFD study was conducted to further validate the above findings. Fig. 15 shows the distribution of absorption coefficients along the axis of the RSC. The absorption coefficient increases from the inlet to the outlet, mainly because the temperature decreases as the heat recovery proceeds. The absorption coefficient of syngas increases with the increase of absorbing gas components. There is a significant difference in the absorption coefficients of syngas with different absorption gas components. Fig. 16(a) shows the heat recovery efficiency of the RSC, which is defined as the ratio of the heat absorbed by the steam to the heat of the inlet syngas. The trend is generally consistent with Fig. 14. When the absorbing gas fraction is low, the variation in heat recovery efficiency is huge. When the absorbing gas fraction increases further to more than 10%, the growth trend of heat recovery efficiency slows down. Fig. 16(b) exhibits that the steam output of the RSC shows a similar

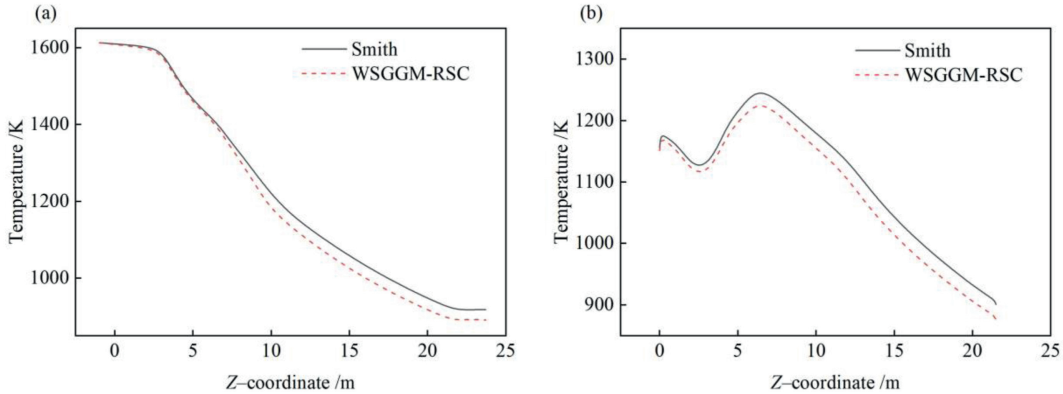

Fig. 11. Comparisons of temperature distributions along the axial direction of different models: (a) in the axis, (b) at a radial distance of 0.05 m from the wall.

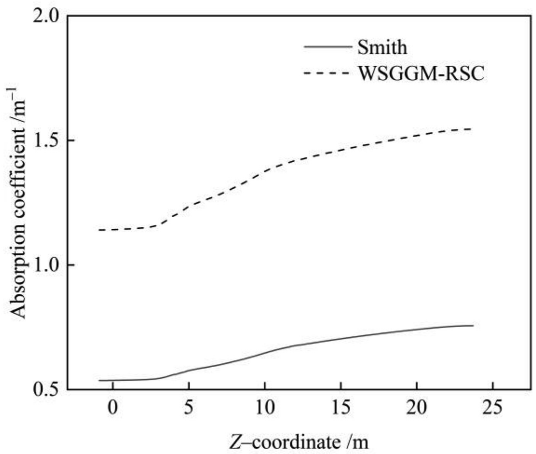

Fig. 12. Absorption coefficient distributions of gas in the axis.

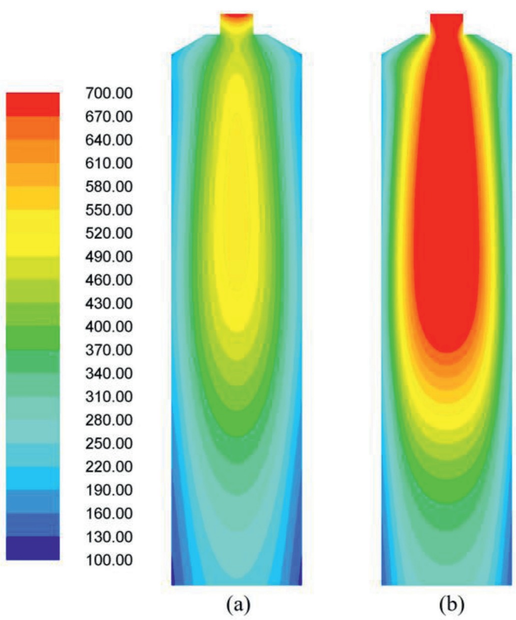

Fig. 13. Incident radiation contours in the center section of the RSC (unit kW·m^{-2}): (a) Smith's model, (b) WSGGM-RSC.

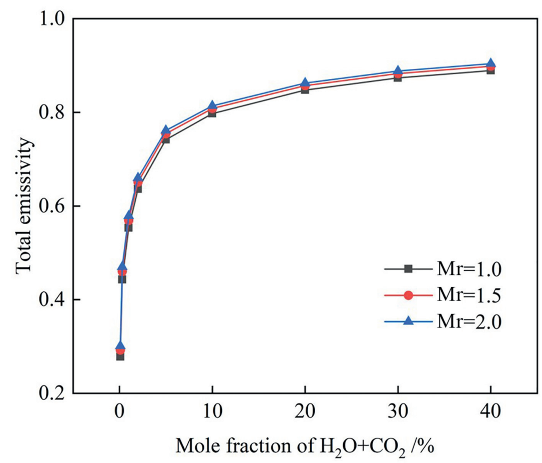

Fig. 14. Relationships between total emissivity calculated by WSGGM-RSC and syngas components: p = 6.5 MPa, T = 1300 K, l = 2.5 m.

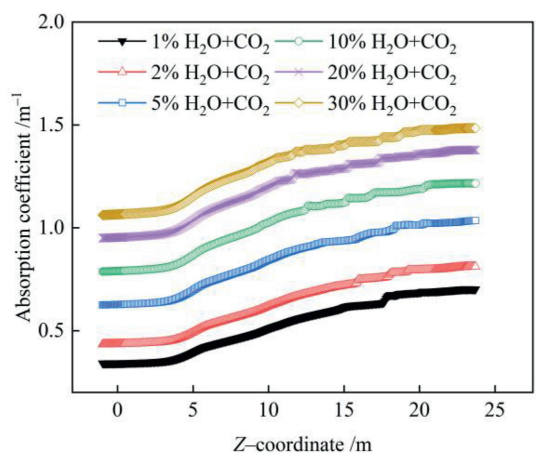

Fig. 15. Absorption coefficients in the axis of the RSC under different syngas components.

trend. The variations of the heat recovery efficiency and steam flow rate are relatively smooth compared to the variation of the total emissivity calculated by WSGGM-RSC. This is mainly because heat

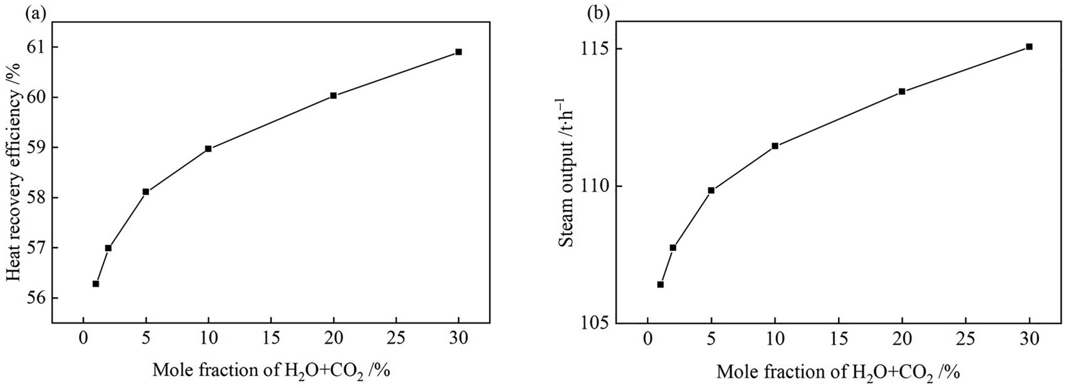

Fig. 16. Heat recovery capability of the RSC: (a) heat recovery efficiency, (b) steam flow rate.

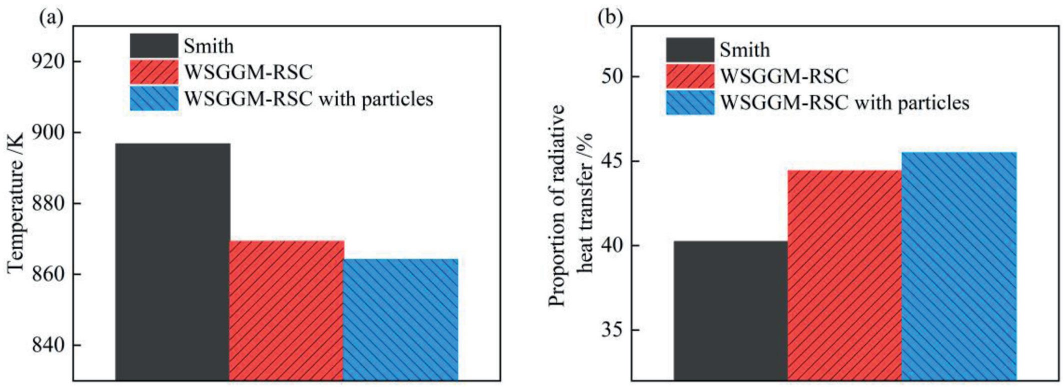

Fig. 17. Comparisons of results calculated by different models: (a) outlet temperature, (b) proportion of radiative heat transfer.

transfer modes other than radiative heat transfer are also considered in CFD research.

4.2.3. Effect of particles on heat transfer behavior in an RSC

Fig. 17 compares the outlet temperature and the proportion of radiative heat transfer under different simulation conditions at the time of start-up. After considering the influence of particles, the outlet temperature decreased by 5 K only, and the proportion of radiative heat transfer increased by 1.1%. However, it does not mean that the impact of particles on heat transfer is minimal. As shown in Fig. 9, the injection of particles leads to more heat being recovered, increasing the steam output by 2.7 t·h^{-1}. Particles contain a certain amount of latent and sensible heat, leading to an increase in the total heat input. Therefore, considering the contribution of particles to heat transfer leads to a more accurate calculation.

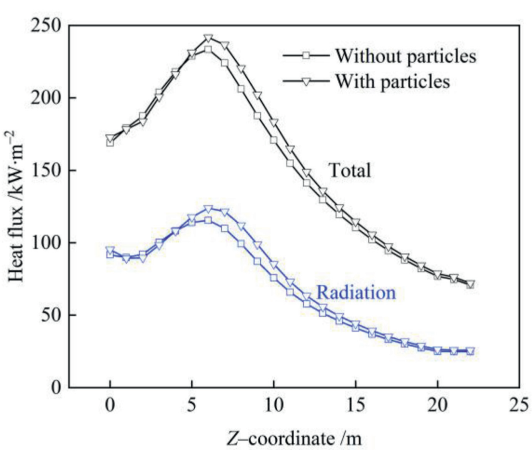

Fig. 18. Total and radiative wall heat fluxes along the axial direction.

Fig. 18 shows the distribution of wall heat flux along the axial direction. It can be seen that the peak of heat flux is located at $Z = 6$ m, which is at the end of the jet core. In this section, the radiative heat flux reaches over 120 kW·m^{-2}, and the total heat flux reaches over 230 kW·m^{-2}. In the lower half of the RSC, the gas temperature decreases steadily, resulting in a decrease in the temperature difference between the gas and the water wall. At the same time, the gas velocity is low in the plug flow area, leading to a decrease in convective heat transfer efficiency. Therefore, the radiative heat flux and total heat flux decrease along the axial direction. After considering the influence of particles, the difference in heat flux mainly occurs near the peak, and the value of the difference is 5–10 kW·m^{-2}.

Fig. 19 shows the distribution of particle concentration and absorption coefficient within RSC. In the axis, the absorption coefficient of the particles is generally higher than that of the gas. The particles are mainly gathered on the axis, which leads to a high absorption coefficient. A few particles may deviate from the axis due to turbulent diffusion and other effects. In the area far from the axis, the absorption coefficient of particles significantly decreases due to low concentration. Therefore, the particle absorption coefficient at 1 m from the axis is much lower than that in the axis. In general, the particle concentration inside RSC is high, and the impact of particles on radiation cannot be ignored. Especially near the axis, particles contribute more to radiation than gas.

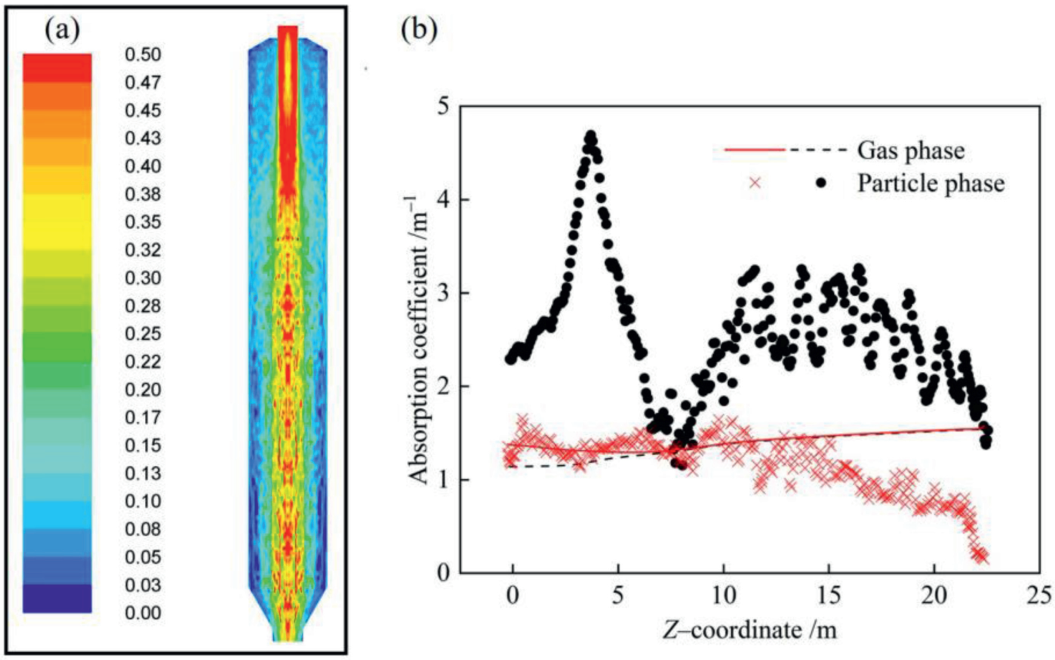

Fig. 19. Particle radiation: (a) particle concentration (unit kg·m^{-3}), (b) comparison of gas and particle absorption coefficients (black pattern represents values in the axis and red pattern represents values at 1 m from the axis).

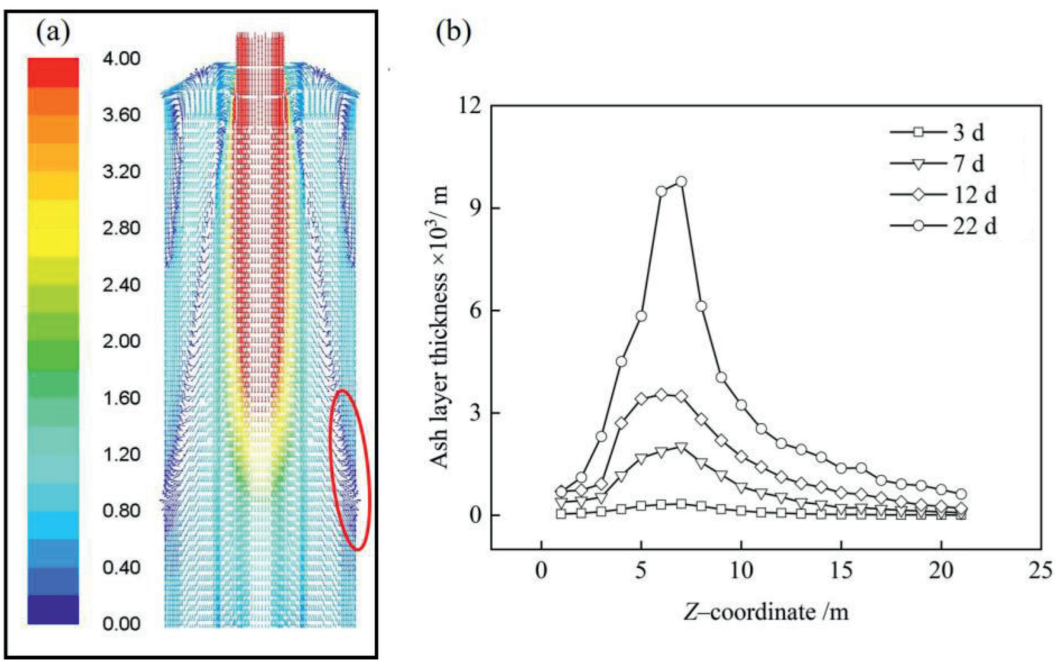

Fig. 20. Ash accumulation on the wall: (a) velocity vector on symmetry (unit m·s^{-1}), (b) ash layer thickness on the circumferential wall.

Accurate prediction of particle deposition is crucial for RSC simulation. In the CVM model, it is believed that the deposition process is related to particles' velocity. As shown in Fig. 20, particles tend to deposit near the end of the jet core. Correspondingly, the ash layer thickness at $Z = 6$ m is the largest, reaching a thickness of 10 mm after 22 days of operation. Fig. 20(a) indicates that the gas velocity near the wall at $Z = 6$ m is relatively lower due to backflow. The low velocity not only leads to a greater chance of particle adhesion after hitting the wall but also decreases the shear stress near the wall, resulting in a larger ash layer thickness.

With the operation of RSC, ash accumulation will greatly affect the heat transfer performance. The variations of outlet temperature and steam output with operating time are shown in Fig. 21. When the operating time is about 20 days, the steam production tends to stabilize. At this time, the outlet temperature has increased to over 1100 K. When the operating time is

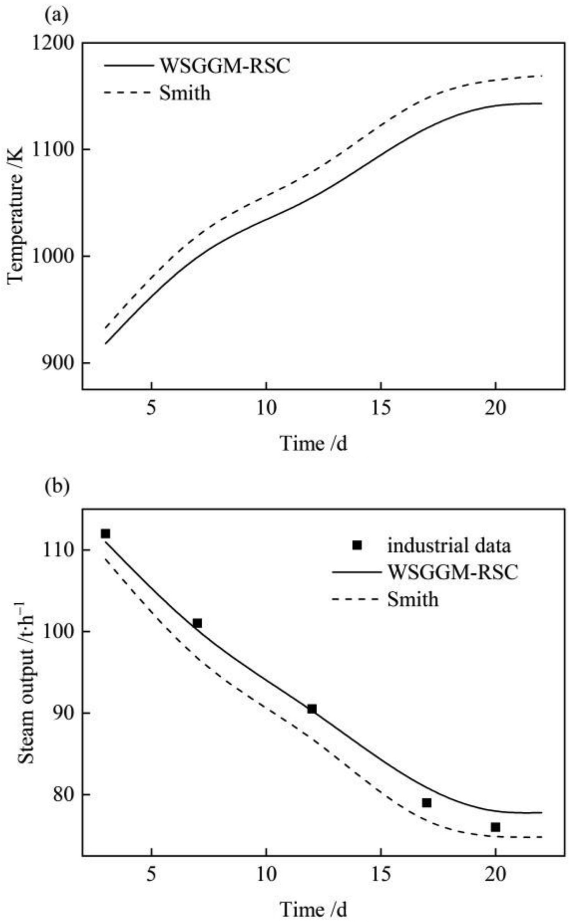

Fig. 21. The variations of outlet syngas temperature and steam output with operating time.

short, the predictions of the CVM model are relatively accurate. However, as the operating time increases, the accuracy of the model decreases. This is probably owing to the CVM underestimating the thickness of the ash layer on the lower half section of the RSC. This requires further research to develop a more accurate adhesion model.

5. Conclusions

In this work, a new WSGGM named WSGGM-RSC is developed, and the validity of the model is verified. The radiative properties of gas, different gas components, and particles are studied. Some reliable conclusions are summarized.

The new model shows a high accuracy both in comparison with benchmarks and industrial data. The deviation of the total emissivity calculated by the new model is significantly reduced compared to traditional models under the working conditions of the RSC. Compared to Smith's model, WSGGM-RSC is more accurate in calculations. It is recommended to use the WSGGM-RSC in RSC simulation calculations.

The gas components have a significant effect on the heat recovery capacity of the RSC. It can be assumed that as the absorbing gas fraction decreases, the weakening trend of the heat recovery capacity of the RSC becomes more obvious. This effect must get attention especially when the mole fraction of $H_2O + CO_2$ is reduced to less than 10%.

The contribution of fly ash particles to the radiation in the RSC is not negligible. Fly ash particles have large sensible heat and strong radiative capacity, especially near the axis. After considering the influence of particles, the changes in outlet temperature and the proportion of radiative heat transfer are small, while the change in steam output is significant. Particles have a significant impact on the wall heat flux at the end section of the jet core (near $Z = 6$ m). Particle deposition greatly weakens the wall heat transfer performance. Due to deposition, steam output has decreased by more than 30% after 20 days of operation.

Declaration of Interest

We declare that we have no financial and personal relationships with other people or organizations that can inappropriately influence our work, there is no professional or other personal interest of any nature or kind in any product, service and/or company that could be construed as influencing the position presented in, or the review of, the manuscript entitled " Influence of syngas components and ash particles on the radiative heat transfer in a Radiant Syngas Cooler".

Acknowledgements

This work was supported by the National Natural Science Foundation of China (21878082).

References

[1] F.C. Wang, G.S. Yu, H.F. Liu, W.F. Li, Q.H. Guo, J.L. Xu, Y. Gong, H. Zhao, H.F. Lu, Z.J. Shen, Opposed multi-burner gasification technology: Recent process of fundamental research and industrial application, *Chin. J. Chem. Eng.* 35 (2021) 124–142.
[2] J.L. Xu, Z.H. Dai, H.F. Liu, L.Y. Guo, F. Sun, Modeling of multiphase reaction and slag flow in single-burner coal water slurry gasifier, *Chem. Eng. Sci.* 162 (2017) 41–52.
[3] P.F. Zhang, C.Z. Xu, J.P. Kuang, S.G. Liu, Z.W. Xia, K. Wu, Y.Q. Huang, Investigation on the ash deposition of a radiant syngas cooler using critical velocity model, *Energy Rep.* 6 (2020) 112–126.
[4] M. Husmann, T. Kienberger, C. Zuber, W. de Jong, C. Hochenauer, Application of CaO sorbent for the implementation and characterization of an *in situ* desulfurization steam-blown bubbling fluidized-bed test rig for biomass gasification, *Ind. Eng. Chem. Res.* 54 (21) (2015) 5759–5768.
[5] J.J. Ni, G.S. Yu, Q.H. Guo, Z.H. Dai, F.C. Wang, Modeling and comparison of different syngas cooling types for entrained-flow gasifier, *Chem. Eng. Sci.* 66 (3) (2011) 448–459.
[6] J.Y. Qiu, Q.H. Guo, J.L. Xu, Y. Gong, G.S. Yu, Numerical study on heat transfer and thermal stress of the upper cone membrane wall in radiant syngas cooler, *Appl. Therm. Eng.* 169 (2020) 114845.
[7] C. Higman, S. Tam, Advances in coal gasification, hydrogenation, and gas treating for the production of chemicals and fuels, *Chem. Rev.* 114 (3) (2014) 1673–1708.
[8] G.S. Yu, J.J. Ni, Q.F. Liang, Q.H. Guo, Z.J. Zhou, Modeling of multiphase flow and heat transfer in radiant syngas cooler of an entrained-flow coal gasification, *Ind. Eng. Chem. Res.* 48 (22) (2009) 10094–10103.
[9] L. Wang, J.Y. Qiu, Q. He, Q.H. Guo, J.L. Xu, L. Ding, G.S. Yu, Performance evolution of industrial radiant syngas cooler with radiation screens using numerical simulation, *Can. J. Chem. Eng.* 101 (1) (2023) 492–503.
[10] X.B. Li, Y. Gong, Z.J. Zhou, Z.H. Dai, G.S. Yu, Simulation of radiant syngas coolers and comparison with various arrangements of the entrained-flow gasifier, *Chem. Eng. Technol.* 39 (8) (2016) 1457–1467.
[11] L. Wang, J.L. Xu, J.T. Wei, Q.H. Guo, Y. Gong, G.S. Yu, Numerical simulation of radiant syngas cooler with different connection to entrained-flow gasifier, *Appl. Therm. Eng.* 201 (2022) 117804.
[12] J.Y. Qiu, Q.H. Guo, J.T. Wei, J.L. Xu, Y. Gong, G.S. Yu, Numerical simulation of heat transfer and a forging plate structure in a radiant syngas cooler with radiation screens, *Ind. Eng. Chem. Res.* 59 (37) (2020) 16483–16491.
[13] W.W. Xuan, Y.Q. Zhang, J.S. Zhang, Chemistry variation of slag and the layered characteristics of deposits in an industrialized entrained-flow gasifier system with radiant syngas cooler, *Energy* 260 (2022) 124942.
[14] Y. Xiong, Y.H. Liu, Y. Guan, H.Z. Liu, S.J. Geng, Numerical study on dynamic ash deposition and heat transfer characteristics of radiant syngas cooler, *Energy* 261 (2022) 125252.
[15] B. Wang, J.Y. Qiu, Q.H. Guo, Y. Gong, J.L. Xu, G.S. Yu, Numerical simulations of solidification characteristics of molten slag droplets in radiant syngas coolers for entrained-flow coal gasification, *ACS Omega* 6 (31) (2021) 20388–20397.

[16] T.F. Smith, Z.F. Shen, J.N. Friedman, Evaluation of coefficients for the weighted sum of gray gases model, *J. Heat Transf.* 104 (4) (1982) 602–608.
[17] C.G. Yin, L.C.R. Johansen, L.A. Rosendahl, S.K. Kær, New weighted sum of gray gases model applicable to computational fluid dynamics (CFD) modeling of oxy–fuel combustion: Derivation, validation, and implementation, *Energy Fuels* 24 (12) (2010) 6275–6282.
[18] R. Johansson, K. Andersson, B. Leckner, H. Thunman, Models for gaseous radiative heat transfer applied to oxy-fuel conditions in boilers, *Int. J. Heat Mass Transf.* 53 (1–3) (2010) 220–230.
[19] T. Kangwanpongpan, F.H.R. França, R. Corrêa da Silva, P.S. Schneider, H.J. Krautz, New correlations for the weighted-sum-of-gray-gases model in oxy-fuel conditions based on HITEMP 2010 database, *Int. J. Heat Mass Transf.* 55 (25–26) (2012) 7419–7433.
[20] X.F. Wu, W.D. Fan, S.L. Liu, J. Chen, H. Guo, Z. Liu, A new WSGGM considering CO in oxy-fuel combustion: A theoretical calculation and numerical simulation application, *Combust. Flame* 227 (2021) 443–455.
[21] K. Uebel, U. Guenther, F. Hannemann, U. Schiffers, H. Yilmaz, B. Meyer, Development and engineering of a synthetic gas cooler concept integrated in a Siemens gasifier design, *Fuel* 116 (2014) 879–888.
[22] Y. Zhang, K. Yue, X.R. Zhang, X.X. Zhang, Deposition characteristics of particles in backward-facing step flow and a radiant syngas cooler, *Case Stud. Therm. Eng.* 43 (2023) 102799.
[23] J.L. Xu, H. Zhao, Z.H. Dai, H.F. Liu, F.C. Wang, Numerical simulation of opposed multi-burner gasifier under different coal loading ratio, *Fuel* 174 (2016) 97–106.
[24] T. Matamba, S. Iglauer, A. Keshavarz, A progress insight of the formation of hydrogen rich syngas from coal gasification, *J. Energy Inst.* 105 (2022) 81–102.
[25] J.X. An, X.J. Luo, Numerical simulation of ash erosion in the selective catalytic reduction catalyst of power plant boiler, *Energy Rep.* 8 (2022) 1313–1321.
[26] J.J. Ni, G.S. Yu, Q.H. Guo, Q.F. Liang, Z.J. Zhou, Experimental and numerical study of the flow field and temperature field for a large-scale radiant syngas cooler, *Ind. Eng. Chem. Res.* 49 (9) (2010) 4452–4461.
[27] Y.X. Wu, J.S. Zhang, P.J. Smith, H. Zhang, C. Reid, J.F. Lv, G.X. Yue, Three-dimensional simulation for an entrained flow coal slurry gasifier, *Energy Fuels* 24 (2) (2010) 1156–1163.
[28] C. Han, Y.M. Situ, B. Zhu, J.L. Xu, X.L. Guo, H.F. Liu, Study of reaction and flow characteristics in multi-nozzle pulverized coal gasifier with co-processing of wastewater, *CIESC J* 74 (8) (2023) 3266–3278. (in Chinese)
[29] B. Wang, J.Y. Qiu, Q.H. Guo, X. Luo, Y. Gong, J.L. Xu, G.S. Yu, Numerical study on the effects of homogeneous reactions on the composition distributions of syngas in radiant syngas cooler, *Appl. Therm. Eng.* 210 (2022) 118307.
[30] G. Krishnamoorthy, A computationally efficient P_1 radiation model for modern combustion systems utilizing pre-conditioned conjugate gradient methods, *Appl. Therm. Eng.* 119 (2017) 197–206.
[31] H.Q. Chu, F. Ren, Y. Feng, M.Y. Gu, S. Zheng, A comprehensive evaluation of the non-gray gas thermal radiation using the line-by-line model in one- and two-dimensional enclosures, *Appl. Therm. Eng.* 124 (2017) 362–370.
[32] C.B. Qi, S. Zheng, H.C. Zhou, Calculations of thermal radiation transfer of C_2H_2 and C_2H_4 together with H_2O, CO_2, and CO in a one-dimensional enclosure using LBL and SNB models, *J. Quant. Spectrosc. Radiat. Transf.* 197 (2017) 45–50.
[33] Y.J. Sun, S. Zheng, F.S. Liu, Non-gray gas and soot radiation heat transfer to a spherical fuel particle in combustion scenarios, *Int. Commun. Heat Mass Transf.* 128 (2021) 105640.
[34] L.S. Rothman, I.E. Gordon, R.J. Barber, H. Dothe, R.R. Gamache, A. Goldman, V.I. Perevalov, S.A. Tashkun, J. Tennyson, HITEMP, the high-temperature molecular spectroscopic database, *J. Quant. Spectrosc. Radiat. Transf.* 111 (15) (2010) 2139–2150.
[35] M.H. Bordbar, G. Węcel, T. Hyppänen, A line by line based weighted sum of gray gases model for inhomogeneous CO_2–H_2O mixture in oxy-fired combustion, *Combust. Flame* 161 (9) (2014) 2435–2445.
[36] A.H. Al-Abbas, J. Naser, D. Dodds, CFD modelling of air-fired and oxy-fuel combustion of lignite in a 100 kW furnace, *Fuel* 90 (5) (2011) 1778–1795.
[37] M.J. Yu, S.W. Baek, J.H. Park, An extension of the weighted sum of gray gases non-gray gas radiation model to a two phase mixture of non-gray gas with particles, *Int. J. Heat Mass Transf.* 43 (10) (2000) 1699–1713.
[38] R.I. Backreedy, L.M. Fletcher, L. Ma, M. Pourkashanian, A. Williams, Modelling pulverised coal combustion using a detailed coal combustion model, *Combust. Sci. Technol.* 178 (4) (2006) 763–787.
[39] F.C. Lockwood, S.A. Rizvi, N.G. Shah, Comparative predictive experience of coal firing, *Proc. Inst. Mech. Eng. C* 200 (2) (1986) 79–87.
[40] L. Ma, M. Gharebaghi, R. Porter, M. Pourkashanian, J.M. Jones, A. Williams, Modelling methods for co-fired pulverised fuel furnaces, *Fuel* 88 (12) (2009) 2448–2454.
[41] K.C. Mills, J.M. Rhine, The measurement and estimation of the physical properties of slags formed during coal gasification: 2. Properties relevant to heat transfer, *Fuel* 68 (7) (1989) 904–910.
[42] C.G. Yin, On gas and particle radiation in pulverized fuel combustion furnaces, *Appl. Energy* 157 (2015) 554–561.
[43] A.G. Konstandopoulos, Particle sticking/rebound criteria at oblique impact, *J. Aerosol Sci.* 37 (3) (2006) 292–305.
[44] B. Ding, X. Zhu, H. Wang, X.Y. He, Y. Tan, Numerical investigation on phase change cooling and crystallization of a molten blast furnace slag droplet, *Int. J. Heat Mass Transf.* 118 (2018) 471–479.